Volume 3
Number 3
May 2025
Pages 351–582

EES Catalysis

rsc.li/EESCatalysis

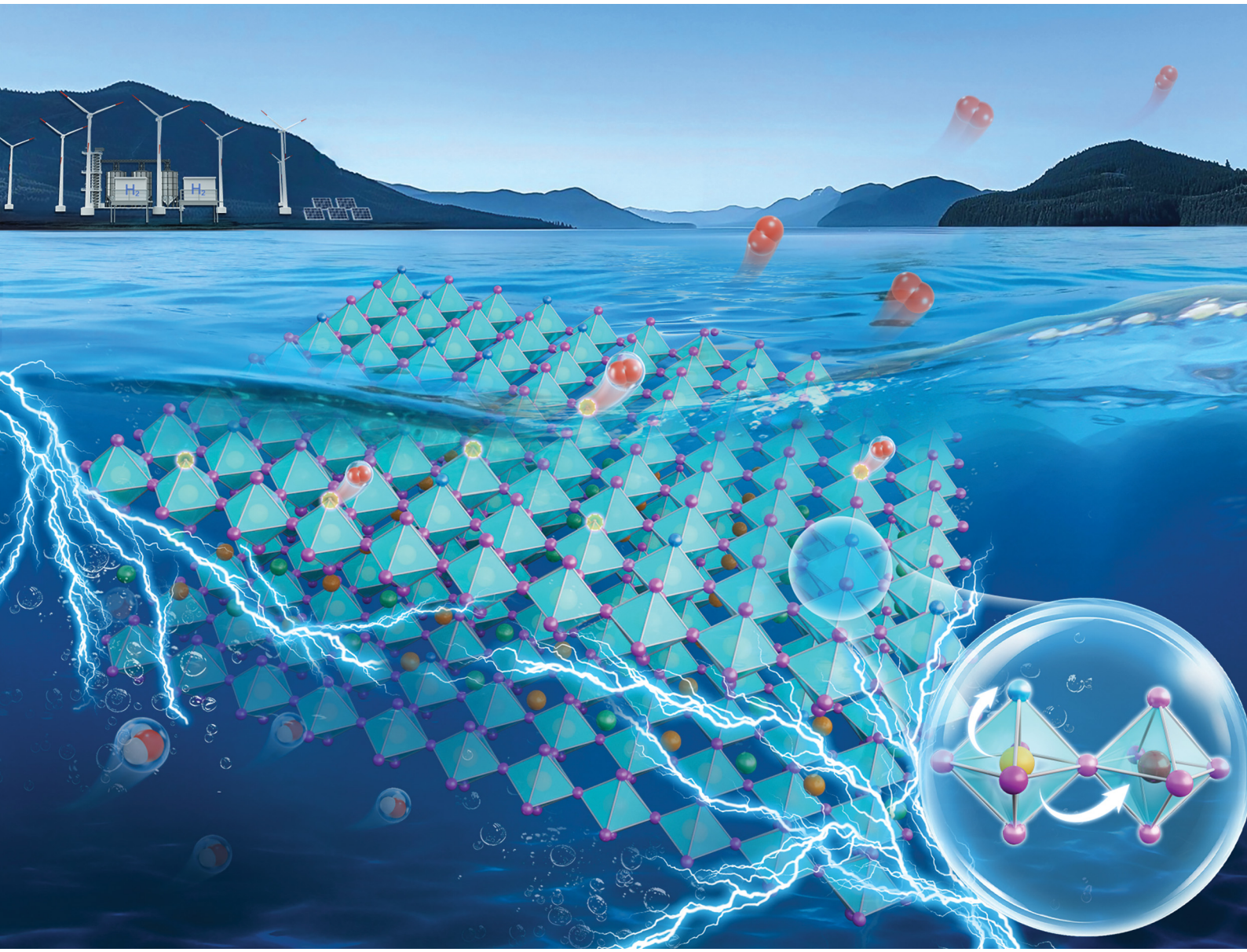

ISSN 2753-801X

ROYAL SOCIETY OF CHEMISTRY

PAPER

Zongyuan Wang, Huan Pang, Feng Yu *et al.*
A plasma-triggered N–Co–O–Fe motif in $Co(OH)_2$ for efficient electrocatalytic oxygen evolution

EES Catalysis

PAPER

View Article Online
View Journal | View Issue

Cite this: *EES Catal.*, 2025, 3, 407

A plasma-triggered N–Co–O–Fe motif in $Co(OH)_2$ for efficient electrocatalytic oxygen evolution†

Qian Yang,‡[a] Yaao Li,‡[a] Yaoxin Wu,[a] Yuxiang Li,[a] Chenxia Yang,[a] Lili Ban,[a] Yunxia Zhao,[a] Bin Dai,[a] Gang Wang,[a] Yongsheng Li,[a] Jinli Zhang,[b] Zongyuan Wang,*[a] Huan Pang*[c] and Feng Yu*[a]

Received 14th December 2024,
Accepted 24th January 2025

DOI: 10.1039/d4ey00280f

rsc.li/eescatalysis

The rational design and synthesis of oxygen evolution reaction (OER) electrocatalysts remain critical challenges for water electrolysis in hydrogen production. This study used a strategy to activate the lattice oxygen mechanism (LOM) pathway in $Co(OH)_2$ through uniform co-doping with metallic Fe and nonmetallic N, thereby forming N–Co–O–Fe moieties at the Fe,N–$Co(OH)_x$ interface. The synergistic effects of Fe and N accelerated electron redistribution from Co to Fe atoms, promoting the formation of active high-valent Co(IV) and stimulating lattice oxygen activation. The intrinsic activity of $Co(OH)_2$ was enhanced. The as-synthesized Fe,N–$Co(OH)_x$ exhibited exceptional performance, with high mass activity (1705 A g_{metal}^{-1}) and turnover frequency (2.521 s^{-1}), surpassing those of W,N–$Co(OH)_x$ by 80.4 and 57 times (21.2 A g_{metal}^{-1} and 0.044 s^{-1}), respectively. *In situ* spectroscopy and ^{18}O isotope-labeled differential electrochemical mass spectrometry confirmed that Fe,N–$Co(OH)_x$ achieved direct intramolecular lattice oxygen coupling *via* the LOM pathway during the OER process. Density functional theory calculations revealed that Fe and N co-doping synergistically modulated the d-band center of Co in Fe,N–$Co(OH)_x$, reducing the energy barrier for OO* desorption to form oxygen vacancies. The proposed method facilitated the preparation of heteroatom-doped hydroxide catalysts to activate the LOM pathway in the OER by co-regulating multiple defects.

Broader context

The generation of hydrogen through electrochemical water splitting is considered a highly promising approach for harvesting energy and alleviating intermittent availability issues associated with renewable energy sources. However, the overall efficiency of water splitting is strikingly hampered by the sluggish kinetics involved in the anodic oxygen evolution reaction (OER). The lattice oxygen oxidation mechanism (LOM) could enable direct *O–O* coupling, thus providing more efficient OER processing. Construction of "M–O–M" moieties at nanoscale interfaces could accelerate electron redistribution and stimulate direct coupling of intramolecular lattice oxygen. In this study metallic Fe and nonmetallic N co-doped $Co(OH)_2$ (Fe,N–$Co(OH)_x$) was successfully synthesized through plasma discharge in water. The co-doping with metallic Fe and nonmetallic N facilitated the formation of N–Co–O–Fe moiety molecules at the Fe,N–$Co(OH)_x$ interface, accelerated electron redistribution from Co to Fe atoms, facilitated the formation of active high-valent Co(IV) and triggered the LOM pathway. This work provides a good reference for the rational design of effective OER catalysts for water electrolysis.

1. Introduction

Electrocatalytic water splitting can facilitate hydrogen production, thereby offering a solution to the impending global energy crisis by converting electrical energy into chemical energy.[1,2] However, the oxygen evolution reaction (OER) component of water splitting ($4OH^- \rightarrow O_2 + 2H_2O + 4e^-$) involves a complex four-electron–proton transfer process. This results in slow kinetics and requires a substantial overpotential. Efficient catalysts must be developed to lower the OER's kinetic barrier to enhance water-splitting efficiency. Unlike noble-metal catalysts (*e.g.*, Ru, Ir, and Pt), which are scarce, costly, and have

[a] *Key Laboratory for Green Processing of Chemical Engineering of Xinjiang Bingtuan, School of Chemistry and Chemical Engineering, Shihezi University, Shihezi 832003, China. E-mail: yufeng05@mail.ipc.ac.cn, zywang@shzu.edu.cn*
[b] *School of Chemical Engineering & Technology, Tianjin University, Tianjin 300384, China*
[c] *School of Chemistry and Chemical Engineering, Yangzhou University, Yangzhou 225009, Jiangsu, P. R. China. E-mail: panghuan@yzu.edu.cn*

† Electronic supplementary information (ESI) available. See DOI: https://doi.org/10.1039/d4ey00280f

‡ These authors contributed equally to this work.

limited durability, earth-abundant 3d transition-metal hydroxides and hydroxyl oxides (*e.g.*, Fe, Ni, and Co) offer comparable electrochemical performances at a lower cost. This renders large-scale industrial water splitting feasible.[3] These materials have been reported to follow two primary OER pathways: the conventional adsorbate evolution mechanism (AEM) and the lattice oxygen oxidation mechanism (LOM).[4–6] In the conventional AEM, the adsorption strength is closely associated with multiple adsorption intermediates, thereby resulting in a theoretical overpotential of 0.37 V.[7] The LOM pathway, which is kinetically favorable, reduces the limiting energy barrier using ligand holes for direct lattice oxygen coupling. Consequently, catalysts operating through the LOM mechanism can achieve superior OER performance.[8] The primary challenge, however, lies in manipulating the catalytic interface to ensure that hydroxide materials follow the LOM pathway.

Heteroatom doping can effectively activate the LOM pathway.[9–11] Wang *et al.* incorporated Zn^{2+} into CoOOH, while Hou *et al.* doped Cu into CoFe-layered double hydroxides (LDH).[12,13] Incorporating Zn^{2+} facilitated the formation of accessible non-bonded oxygen states and enhanced Co–O covalency, whereas Cu doping promoted intramolecular electron transfer, activating the LOM pathway. In addition, heteroatom doping can induce interfacial catalysis at the nanoscale, consequently altering the electronic structure of the catalyst, facilitating lattice oxygen activation, and modifying catalytic activity.[14–16] Ou *et al.* introduced Ga^{3+} into Co_3O_4 to create Co^{2+}–O–Co^{3+} motifs, which successfully activated lattice oxygen.[17] Similarly, Yang *et al.* used O species in CoFe-PBA, forming Co–O–Fe motifs that enhanced the lattice oxygen activation and improved OER performance.[14] Liu *et al.* introduced S and FeOOH on $Co(OH)_2$ nanoneedle arrays, thereby inducing Co–O–Fe motifs at the heterogeneous interface, accelerating electron transfer, and triggering the LOM pathway.[18] Thus, the construction of ''M–O–M'' motifs at nanoscale interfaces accelerates electron redistribution and enhances metal–O covalency, consequently stimulating direct intramolecular lattice oxygen coupling. However, Chen *et al.* highlighted that the formation of oxygen vacancies (O_v) is the rate-limiting step of the LOM pathway.[19] In many cases, the removal of OO* or OOH* intermediate species occurs in this step. Thus, the key challenge in activating the LOM pathway is facilitating lattice oxygen participation in the OER to form O_v. This necessitates the maintenance of a high O exchange capacity at the O_v site and a robust H exchange capacity following the occupation of the site by OH* or OOH*.

With its LDH groups and hydrotalcite-like structures, α-$Co(OH)_2$ can expose several surface-active catalytic sites and provide sufficient structural flexibility for the LOM.[20] However, α-$Co(OH)_2$ has a high O_v formation energy and is not naturally inclined to follow the LOM pathway. Moreover, its limited electrical conductivity further impedes charge injection and extraction during O_2 evolution. To enhance its activity, Fe species are commonly incorporated with α-$Co(OH)_2$'s to form highly active OER catalysts, such as CoFe-LDH and Fe_2O_3/$Co(OH)_2$.[21–23] Fe can effectively modify the hydrogen exchange capacity of α-$Co(OH)_2$ for OOH and OH groups,[24–26] while N-doping can adjust the conductivity and electronic structure of $Co(OH)_2$.[27,28] Nevertheless, to the best of our knowledge, the activation of the LOM pathway in $Co(OH)_2$ has not been reported. Furthermore, studies have indicated that co-doping with metals and nonmetals can effectively enhance intrinsic conductivity and modulate electronic interactions, thereby improving the intrinsic catalytic activity.[10,29,30] However, simultaneously realizing metallic and nonmetallic doping in a single-step process remains challenging. This study aimed to identify an optimal metallic and nonmetallic co-doped structure that could activate the LOM mechanism and improve electron transfer capabilities.

This study proposed a rapid and environmentally friendly method for synthesizing metallic Fe and nonmetallic N co-doped $Co(OH)_2$ (*i.e.*, Fe,N–$Co(OH)_x$) with abundant O_v *via* plasma discharge at the gas–water interface. In an aqueous solution, Co^{2+} and 2-methyl-1*H*-imidazole (2-MI) facilitated the formation of N-doped $Co(OH)_2$, while Fe rods, used as discharge electrodes, served as the Fe source. The Fe atoms were uniformly sputtered into the N-doped $Co(OH)_2$. By adjusting the Co/2-MI ratio, Fe,N–$Co(OH)_x$ and Fe-doped ZIF67 (Fe-ZIF67) were synthesized. W,N–$Co(OH)_x$ was also synthesized as a control. Co-doping with Fe and N promoted the formation of N–Co–O–Fe moieties at the Fe,N–$Co(OH)_x$ interface, thereby modulating electron redistribution between Co and Fe and optimizing the adsorption and desorption of oxygen intermediates. This enhanced the intrinsic activity of $Co(OH)_2$. *In situ* ATR-FTIR, *in situ* ^{18}O isotope-labeled differential electrochemical mass spectrometry (DEMS), and *in situ* Raman spectroscopy confirmed that Fe and N co-doping activated lattice oxygen. This established the LOM pathway as the primary reaction mechanism and facilitated the formation of active high-valent Co(IV) species. Furthermore, *in situ* electrochemical impedance analysis and density functional theory (DFT) calculations were performed to investigate further the impact of Fe and N co-doping on OER activity and LOM pathway activation.

2. Results and discussion

2.1. Morphology and structure

To achieve the co-doping of Fe and N, a plasma setup (Fig. S1 and S2, ESI†) previously reported for constructing single-atom sites and anionic doping structures (*e.g.*, N, F, P, and B) was used.[31–35] Previous research on N-doped transition-metal-based electrocatalysts has primarily focused on the development of transition-metal nitrides using highly corrosive NH_3 as the nitrogen source. Simultaneously, reports on N-doping under mild conditions remain scarce.[36–39] This plasma treatment in water stabilizes hydroxides and prevents their decomposition into oxides during high-temperature calcination, thereby forming Co–N bonds. The Fe,N-doped $Co(OH)_2$ synthesis is depicted in Fig. S2 (ESI†), demonstrating that Co^{2+} initially coordinated with 2-MI to form Co–N bonds. Following plasma treatment, most of the Co–N bonds are converted to Co–OH, and the 2D

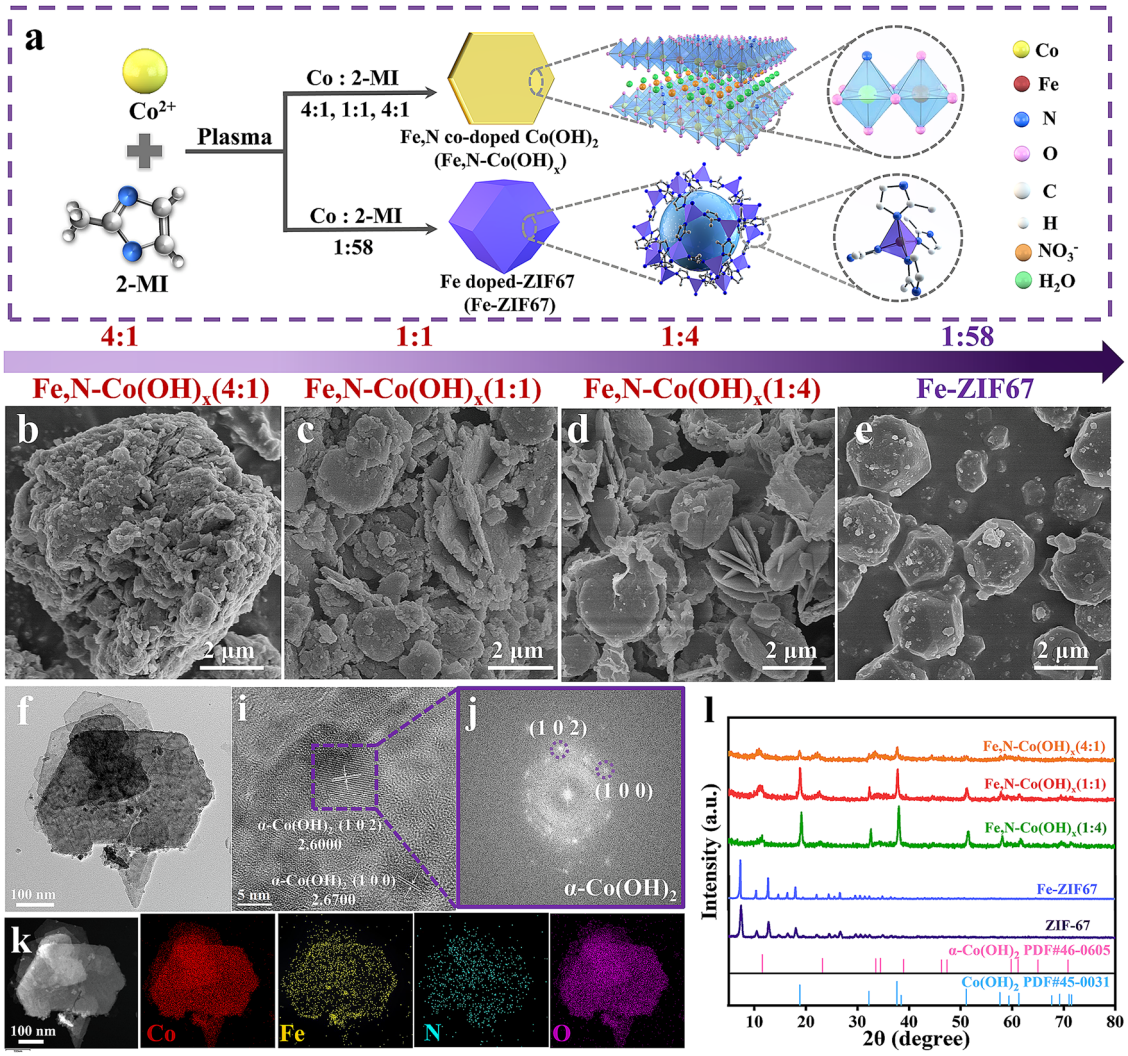

Fig. 1 Preparation process and morphology of electrocatalysts. (a) Schematic of the synthesis of Fe,N co-doped $Co(OH)_2$ (*i.e.*, Fe,N–$Co(OH)_x$) and Fe-doped ZIF67 (*i.e.*, Fe-ZIF67) induced by plasma in water. (b)–(e) SEM images of (b) Fe,N–$Co(OH)_x$ (4 : 1), (c) Fe,N–$Co(OH)_x$ (1 : 1), (d) Fe,N–$Co(OH)_x$ (1 : 4), and (e) Fe-ZIF67. (f)–(k) Morphology and elemental distribution of Fe,N–$Co(OH)_x$ (1 : 1): (f) TEM images, (i) HAADF-STEM images, (j) corresponding FFT pattern, and (k) EDS mapping images. (l) XRD patterns of Fe,N–$Co(OH)_x$ (4 : 1) (orange line), Fe,N–$Co(OH)_x$ (1 : 1) (red line), Fe,N–$Co(OH)_x$ (1 : 4) (green line), and Fe-ZIF67 (purple line).

α-$Co(OH)_2$ is formed as NO^{3-} ions of cobalt nitrate or degradation products are inserted between the Co–OH layers. Fe,N–$Co(OH)_x$ appeared as hexagonal plates in SEM images (Fig. 1b–d). Furthermore, the color of the solution changed from red to yellow and purple following 30 m of plasma discharge when the Co^{2+}/2-MI molar ratio increased from 4 : 1 to 1 : 1 and 1 : 4 (Fig. S4a–c, ESI†). The dark purple Fe-ZIF67, prepared at a Co^{2+}/2-MI ratio of 1 : 58, exhibited an *ortho*-dodecahedral morphology (Fig. 1e and Fig. S4d, ESI†) that was consistent with hydrothermally synthesized ZIF-67 (Fig. S5, ESI†).[40] The Fe doping results were obtained from Fe electrode sputtering. The substitution of Fe with W electrodes produced W,N–$Co(OH)_x$ (1 : 1) as a control sample. The reaction temperature was mild at 79 °C (Fig. S6, ESI†). Thus, this study presented the first report of a one-step synthesis of metallic/nonmetallic (Fe/N) co-doped $Co(OH)_2$ for the OER.

Transmission electron microscopy (TEM) images of Fe,N–$Co(OH)_x$ (1 : 1) revealed a hexagonal plate-like morphology (Fig. 1f), thereby corroborating the SEM findings. The staggered lattice fringes indicated abundant defects[41–43] (Fig. 1i), with measured lattice spacings of 2.60 and 2.67 nm, corresponding to the (102) and (100) planes of α-$Co(OH)_2$, respectively.[44] Fe,N–$Co(OH)_x$ (1 : 1) exhibited polycrystalline characteristics (Fig. 1j). Energy-dispersive spectroscopy (EDS) mapping indicated Co and O as dominant elements, with Fe and N homogeneously distributed throughout the hexagonal plate region. This confirmed uniform co-doping (Fig. 1k). Inductively coupled plasma (ICP) measurements revealed that the Co and Fe contents in Fe,N–$Co(OH)_x$ (1 : 1) were 43.37 wt% and 8.98 wt% (molar ratio of Co/Fe = 4.83), respectively (Table S2, ESI†). Furthermore, W,N–$Co(OH)_x$ (1 : 1) exhibited similar 2D morphology and uniform W,N-doping (Fig. S7 and S8, ESI†).

X-ray diffraction (XRD) analysis confirmed the primary crystal structure of α-$Co(OH)_2$ (JCPDS No. 46-0605) and $Co(OH)_2$ (JCPDS No. 45-0031) (Fig. 1l).[45] When decreasing the Co^{2+}/2-MI ratio from 4 : 1 to 1 : 4, the shape of peaks at 18.8°, 32.2°, 37.7°, and 51.1° became sharper, and the peak intensity enhanced, indicating an increased crystallinity. Fourier transform infrared (FTIR) spectroscopy of Fe,N–$Co(OH)_x$ (4 : 1), (1 : 1), and (1 : 4) exhibited vibration bands at 480, 656, 3447, and 3632 cm^{-1}, corresponding to Co–OH, Co–O, –OH groups of typical α-phase hydroxides, and O–H stretching vibrations of interlayer water, respectively (Fig. S9, ESI†).[45,46] With increasing 2-MI content, the peaks at 480 and 3632 cm^{-1} intensified, indicating increased interlayer OH groups. This was consistent with the XRD results, thereby indicating improved crystallinity as the Co^{2+}/2-MI ratio shifts from 4 : 1 to 1 : 4. The NO_3^- vibration at 1383 cm^{-1} was attributed to interlayer NO_3^-,[47] which disappeared in Fe-ZIF67 and ZIF-67. Increasing the 2-MI ratio to 58 eq., typical for ZIF-67 synthesis,[40] caused the Fe-ZIF67 to exhibit an XRD pattern similar to ZIF-67 (Fig. 1l). The FTIR spectra of Fe-ZIF67 also matched that of ZIF-67 (Fig. S9, ESI†), with peaks between 600 and 1600 cm^{-1} attributed to imidazole ring stretching and bending.[48] Peaks at 425 and 1580 cm^{-1} corresponded to Co–N and C═N stretching of Co/2-MI hybrids. These findings confirmed the synthesis mechanism illustrated in Fig. 1a. Plasma induced Co^{2+}/2-MI reconstitution into N-doped α-$Co(OH)_2$ at low 2-MI concentrations, incorporating NO_3^- into the 2D α-$Co(OH)_2$ interlayer. At higher 2-MI concentrations, the coordination of 2-MI with Co^{2+} facilitated the formation of ZIF-67. The competition between 2-MI and OH^- coordination with Co^{2+} yielded various morphologies. This highlighted the importance of the Co^{2+}/2-MI ratio in synthesizing Fe,N–$Co(OH)_x$.

XPS analysis was conducted to identify the electronic structure and elucidate the chemical states (Fig. S10 and S11, ESI†). The Co 2p spectra of Fe,N–$Co(OH)_x$ are shown in Fig. S11a (ESI†). Two dominant Co $2p_{1/2}$ and Co $2p_{3/2}$ peaks with two shakeup satellites were observed.[46] The peaks at 780.7 and 782.6 eV corresponded to Co^{3+} ($t_{2g}^6e_g^0$) and Co^{2+} ($t_{2g}^6e_g^1$), respectively. Fe,N–$Co(OH)_x$ (1 : 1) contained the highest percentage of Co^{3+} (56.4%) (Table S4, ESI†), which may benefit OER performance.[49] Notably, there was a slightly negative shift (0.3 eV) of the Co $2p_{3/2}$ peak between Fe,N–$Co(OH)_x$ (1 : 1), and Fe-ZIF67 (Fig. S11a, ESI†). This indicated increased electron cloud density around the Co atoms after Fe,N co-doping.[24] The O 1s spectra of Fe,N–$Co(OH)_x$ (1 : 1) exhibited four peaks at 529.9, 530.8, 531.4, and 532.3 eV, attributed to lattice oxygen (metal–O), metal–OH, O_v, and surface-absorption oxygen, respectively (Fig. S11d, ESI†).[13] Fe,N–$Co(OH)_x$ (1 : 1) exhibited the highest O_v content (51.9%). Electron paramagnetic resonance (EPR) confirmed abundant O_v formation (Fig. S12, ESI†),[50] thereby demonstrating that rational Fe,N co-doping facilitated O_v formation. The Fe 2p XPS spectra of Fe,N–$Co(OH)_x$ (1 : 1) was deconvoluted into four main peaks representing Fe^{2+} (711.9 and 722.0 eV) and Fe^{3+} (715.0 and 725.5 eV) with two satellite peaks (718.7 and 733.14 eV, respectively) (Fig. S11b, ESI†).[25] The N 1s spectra of Fe,N–$Co(OH)_x$ (1 : 1) revealed five N species: pyridinic N (398.5 eV), Co–N or Co/Fe–N (399.7 eV),[28] pyrrolic-N (400.9 eV), graphitic N (402.8 eV), and NO_3^-(406.7 eV) (Fig. S11c, ESI†). Raman spectra (Fig. S13 and Note 3, ESI†) have been verified and revealed the origin of the metal–N bond. The N–Co–N deformation vibration was clearly observed in the region of 120–195 cm^{-1}. And the C–CH_3 stretching peaks of the 2-MI linker were visible at approximately 674 cm^{-1}, indicating that the Co–N bond in Fe,N–$Co(OH)_x$ originates from 2-MI.[51] Pyridinic and graphitic N, part of the N-doped C, exhibited improved wettability and a strong affinity for water, thereby aiding electron transfer during the OER.[52]

X-ray absorption spectroscopy (XAS) was conducted to analyze the coordination number and multi-defect structures in Fe,N–$Co(OH)_x$ (1 : 1) (Fig. 2a–c and Fig. S14, Table S6, ESI†). A detailed analysis of the pre-peak and main peak in the Co K-edge X-ray absorption near-edge structure (XANES) spectra of Fe,N–$Co(OH)_x$ (1 : 1) was carried out to elucidate the oxidation states, coordination environment and electronic interactions induced by the Fe and N co-doping. The Co K-edge X-ray XANES spectra (Fig. 2a) exhibit the energy absorption edge between CoO and Co_3O_4, confirming a mixed valence state of Co^{2+} and Co^{3+}. The pre-edge peak around 7710 eV corresponds to the Co 1s-3d transition,[53] and a higher pre-edge peak represents a lower centrosymmetry of the octahedron in $Co(OH)_2$. The pre-edge peak intensity of Fe,N–$Co(OH)_x$ (1 : 1) is higher than $Co(OH)_2$, which suggests a lower centrosymmetry of Fe,N–$Co(OH)_x$ (1 : 1) after Fe and N co-doping.[54] Compared with $Co(OH)_2$, the white line (7725 to 7730 eV) of Fe,N–$Co(OH)_x$ (1 : 1) sample is broader and lower intensity, indicating strong electronic interaction after Fe and N co-doping.[55] The Fourier transformed (FT) $k^3\chi(k)$ spectra in R space (Fig. 2b) revealed three scattering paths around absorbing Co ions. The first peak at 1.53 Å corresponded to the Co–O and Co–N first coordination shell.[27] Owing to limited resolution and low N content, differentiating between Co–N and Co–O was challenging.[27] The second peak at 2.5 Å indicated the Co–O–Co(Fe) second coordination shell.[56] Moreover, the coordination bond length and peak intensity of Fe,N–$Co(OH)_x$ (1 : 1) are significantly lower than those of $Co(OH)_2$, which indicates that Fe and N co-doping resulted in the formation of multiple defects.[14] According to the (FT) $k^3\chi(k)$ fitting results and parameters (Fig. 2c and Table S6, ESI†), the *ex situ* Raman experimental (Fig. S13 and Note 3, ESI†) and fitting data showed high consistency, revealing that the Co–N and Co–O coordination numbers (CN) are 2 and 1.5, respectively. Compared to the 6-coordinated metal–O structure in saturated-coordinated $Co(OH)_2$, the first-shell coordination numbers of Fe,N–$Co(OH)_x$ (1 : 1) sum up to 3.5, which is lower than 6. This indicated the presence of abundant O_v,[41,57] which was consistent with XPS and EPR findings. The EXAFS wavelet transform analysis revealed an intensity maximum at 3.5 $Å^{-1}$ owing to Co–N/O scattering (Fig. S14, ESI†). These results indicated that Fe,N co-doping altered the coordination environment in Fe,N–$Co(OH)_x$ (1 : 1), leading to multiple defects (Fe,N co-doping and O_v).

XAS and XPS data revealed that introducing metallic Fe and nonmetallic N substantially modified the valence states,

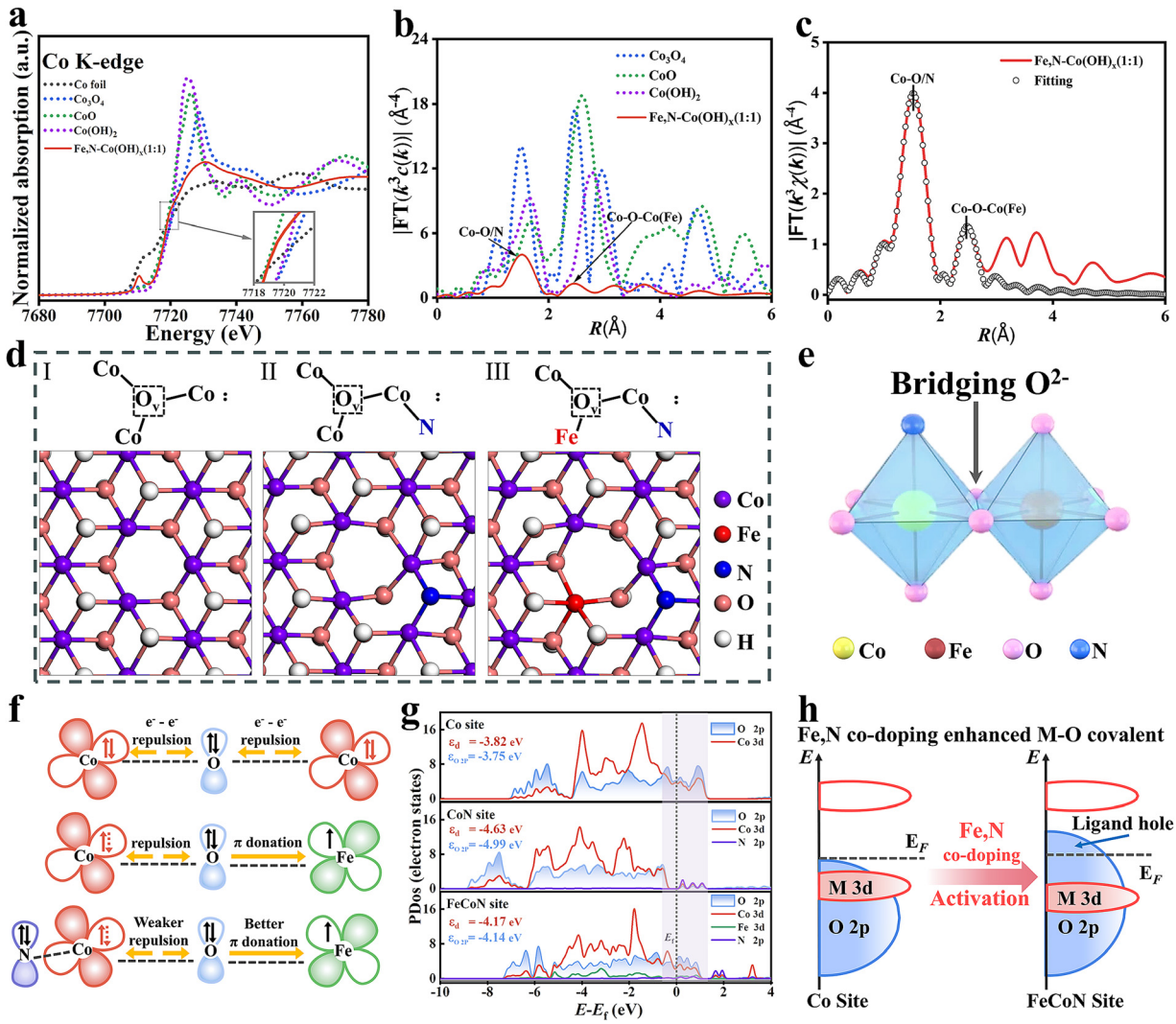

Fig. 2 Effect of Fe,N co-doping on electronic structure. (a–c) XAS characterization of Fe,N–Co(OH)$_x$ (1 : 1): (a) XANES spectra at the Co K-edge. (b) Fourier transform of Co K-edge EXAFS spectra in *R* space. (c) EXAFS fitting results of Co K-edge EXAFS $k^3\chi(k)$ FT spectra. (d) Slab model structure (O_v) diagrams for (I) Co, (II) CoN, and (III) FeCoN sites. (e) Schematic of the N–Co–O–Fe moiety connecting Co and Fe *via* bridging lattice oxygen (O^{2-}). (f) Schematic of PET in the N–Co–O–Fe moiety through bridging O^{2-}. (g) Partial density of states of potential catalytic sites. (h) Illustration of the electronic structure of the metal–O covalent bond.

coordination environments, and electronic structure of the Co atoms. We proposed the Co, CoN, and FeCoN site structures, as illustrated in Fig. 2d. The lattice oxygen between Co and Fe also affected adsorption–desorption properties (Fig. 2d and Fig. S16–S18, ESI†). Typically, O_h-symmetric metal atoms interacted with bridging oxygen (O^{2-}) through π-donation in hydroxide structures, thereby forming M–O–M moieties.[58] In this study, we constructed an N–Co–O–Fe moiety that bridged Co and Fe *via* O^{2-} to examine partial electron transfer (PET) at the interface and electronic coupling between adjacent Co and Fe (Fig. 2e). The d-orbital configurations of Co^{2+} ($t_{2g}^6e_g^1$), Co^{3+} ($t_{2g}^6e_g^0$), and Fe^{3+} ($t_{2g}^3e_g^2$) are depicted in Fig. S15 (ESI†). The t_{2g}-orbitals of Co^{2+} ($t_{2g}^6e_g^1$) and Co^{3+} ($t_{2g}^6e_g^0$) had no unpaired electrons, and their p-orbitals were fully occupied by O^{2-}. This resulted in electron repulsion that hindered the charge transfer (Fig. 2f, top).[56,59] Projected density of states (PDOS) calculations indicated substantial overlap between Co t_{2g}-orbitals and O 2p-orbitals near the Fermi level (−0.5–2 eV), thereby confirming electron transfer from the t_{2g}-orbitals (d_{xy}, d_{yz}, d_{xz}) to bridging O^{2-} (Fig. S16a, top, ESI†).[12] The varying electronic occupancy of Co and Fe d-orbitals can trigger PET through bridging O^{2-} p-orbitals (Fig. 2f, middle),[56,57,60] resulting in double interaction (DEI) between Co and Fe.[61,62] N facilitated electron transport by altering the electronic density at adjacent Co sites.[63] Introducing N at the CoN site substantially reduced the electron density in Co t_{2g}-orbitals and O 2p orbitals near the Fermi level (−0.5–2 eV) (Fig. S16a, middle, ESI†), while co-doping with Fe and N markedly increased it (Fig. S16a, bottom, ESI†). This highlighted the electron-withdrawing properties of N, which decreased the electron density at the adjacent Co sites. With Fe and N coordinated to Co^{2+}/Co^{3+}, the orbitals contained more electrons, facilitating electron transfer between

Co t_{2g} and O 2p-orbitals. This enabled easier electron transfer from Co^{2+}/Co^{3+} to Fe^{3+} *via* bridging O^{2-} (Fig. 2f, bottom). This process facilitated electron redistribution.[59] Benefiting from the electronic modulation of the N–Co–O–Fe moiety, the Fe sites optimize *OH adsorption, while the Co sites are more conducive to O_2 desorption, thus Fe,N–Co(OH)$_x$ is more favorable for starting an OER cycle and oxygen release (Fig. S17, S18 and Note 4, ESI†). The mechanism of the effects of Co and Fe on the absorption of oxygen-containing species will be analyzed in the DFT calculation section. Hence, the intrinsic OER activity of Fe,N–Co(OH)$_x$ could be enhanced through PET within the N–Co–O–Fe moiety.

Moreover, PDOS analysis validated the variation in the electronic structure of the lattice oxygen based on comparisons of the Co, CoN, and FeCoN sites within the N–Co–O–Fe model (Fig. 2d and g). As shown in Fig. 2g, the moderate d-band center of Co (−4.17 eV) at the FeCoN site, compared to the Co (−3.82 eV) and CoN (−4.63 eV) sites, indicated that Fe,N–Co(OH)$_x$ (1 : 1) possessed optimal adsorption and desorption energies for OER intermediates. Fe,N co-doping shifted the metal d-band center downward from −3.82 to −4.17 eV, reducing the charge transfer (Δ) between ε_d and the O 2p-band center ($\varepsilon_{O\,2P}$) from −0.07 to −0.03 eV.[64] This shift facilitated the penetration of the O 2p-band and the formation of ligand holes, which favored the release of lattice oxygen (Fig. 2h). This confirmed the occurrence of lattice oxygen oxidation and enabled the lattice oxygen to function as active sites.[20,64–66] For the FeCoN site, the overlap of the Co 3d, Fe 3d, and lattice O 2p orbitals near the Fermi level (shaded in purple) was substantially increased compared to the Co and CoN sites (Fig. 2g, lower panel). This confirmed a strong interaction between Co and Fe atoms and covalent hybridization with oxygen ligands. In addition, the continuous band structure of Fe,N–Co(OH)$_x$ (1 : 1) around the Fermi level supported high electrical conductivity and enhanced electron transfer. This synergy between Fe and N atoms strengthened the covalency of the metal–O bond, thereby promoting lattice oxygen activation during the OER.[8,12,67] The hybridization of metal 3d and O 2p orbitals improved electron transfer efficiency during OER processes,[68] which facilitated the LOM pathway.

2.2. Electrocatalytic performance

Fe,N–Co(OH)$_x$ (1 : 1) demonstrated better activity than Fe,N–Co(OH)$_x$ (4 : 1) and (1 : 4), indicating an optimal reactant ratio (Fig. S20, ESI†). The Fe,N–Co(OH)$_x$ (1 : 1) catalyst exhibited the lowest overpotential at 10 mA cm^{-2} (η_{10} = 251 mV), substantially lower than that of RuO_2 (363 mV), W,N–Co(OH)$_x$ (1 : 1) (378 mV), and ZIF-67 (386 mV) (Fig. 3a). At current densities of 100 and 300 mA cm^{-2}, Fe,N–Co(OH)$_x$ maintained superior overpotentials of 309 and 345 mV, respectively (Fig. 3b). The Tafel slope for Fe,N–Co(OH)$_x$ (1 : 1) (40 mV dec^{-1}) was notably smaller than those of RuO_2 (88 mV dec^{-1}), W,N–Co(OH)$_x$ (1 : 1) (89 mV dec^{-1}), and ZIF-67 (106 mV dec^{-1}). This confirmed superior reaction kinetics (Fig. 3c). Various doped samples were also investigated for comparison with Fe and N co-doped samples. The OER properties of Ni,N–Co(OH)$_x$, W,N–Co(OH)$_x$, Fe–Co(OH)$_x$, N–Co(OH)$_x$, Co(OH)$_x$ and Fe,N–Co(OH)$_x$ OER properties are compared in Fig. S21 (ESI†). From the results, Fe–Co(OH)$_x$ and Co(OH)$_x$ without N doping, as well as Ni,N–Co(OH)$_x$, W,N–Co(OH)$_x$, N–Co(OH)$_x$ and Co(OH)$_x$ without Fe doping all exhibit poor activities. These comparisons indicated that Fe and N co-doping exerted a synergistic effect on enhancing the OER activity.

To further understand the mechanism governing the high OER activity of Fe,N–Co(OH)$_x$ (1 : 1), impedance spectroscopy (EIS) and intrinsic activity assessments were conducted. The EIS results (Nyquist plots) indicated that Fe,N–Co(OH)$_x$ (1 : 1) exhibited the lowest resistance (2.26 Ω) and efficient proton-coupled electron transfer capability (Fig. S22 and Table S7, ESI†). To elucidate the charge transfer processes at the catalytic interface, the operando EIS test was conducted at various applied biases to track dynamic evolution. The corresponding Bode phase plots illustrate the variation of phase angles with frequency (Fig. 3d and Fig. S23, ESI†). When the voltage was increased from 1.3 V to 1.6 V, the phase angle of Fe,N–Co(OH)$_x$ (1 : 1) decreased significantly in the low and high frequency regions of Bode phase plots (Fig. 3d), indicating rapid electron transport at the electrolyte/electrode interfaces and implying an accelerated interfacial reaction during the electrocatalytic OER process.[69] However, the frequency peak decreases more slowly with increasing bias for W,N–Co(OH)$_x$ (1 : 1) (Fig. S23, ESI†). From the above results, it is confirmed that Fe-doping can promote the electron transfer ability and accelerate surface remodeling at the electrode interface, thus promoting the OER process. The intrinsic OER activity was further evaluated using ECSAs and loading mass to identify active sites. Fe,N–Co(OH)$_x$ (1 : 1) exhibited an ECSA of 110 cm^2, which was larger than that of other samples (Fig. S24, ESI†). The mass activities and turnover frequencies (TOF) at an overpotential of 350 mV were also estimated. Fe,N–Co(OH)$_x$ (1 : 1) exhibited the highest mass activity (1705 A g_{metal}^{-1}) and TOF (2.521 s^{-1}), which were 80.4 and 57 times greater than those of W,N–Co(OH)$_x$ (1 : 1) (21.2 A g_{metal}^{-1} and 0.044 s^{-1}), respectively (Fig. S25 and Table S7, ESI†). Radar plots visually compare the performance of these catalysts. They clearly showed the superior intrinsic activity of Fe,N–Co(OH)$_x$ (1 : 1) (Fig. 3e), confirming that the incorporation of Fe and N enhanced the intrinsic activity of $Co(OH)_2$. A summary of the electrochemical test results is provided in Table S7 (ESI†).

The long-time operational stability of Fe,N–Co(OH)$_x$ (1 : 1) was assessed through chronopotentiometry measurements. The operating potential remained stable, with real-time potentials demonstrating minimal change following 50 h of oxygen evolution (Fig. S26, ESI†). The catalyst durability was further demonstrated at higher current densities of 10, 50, and 100 mA cm^{-2} (Fig. 3f). Stability results showed that Fe,N–Co(OH)$_x$ (1 : 1) requires only ∼1.5 V to drive a current density of 10 mA cm^{-2}, whereas W,N–Co(OH)$_x$ (1 : 1) requires ∼1.65 V (Fig. S27, ESI†), indicating that Fe,N-codoping Co(OH)$_x$ can achieve long-term OER reactions at lower voltages. These results confirmed that Fe,N–Co(OH)$_x$ (1 : 1) exhibited excellent stability in alkaline solutions. Fig. 3j presents a comparison of the OER

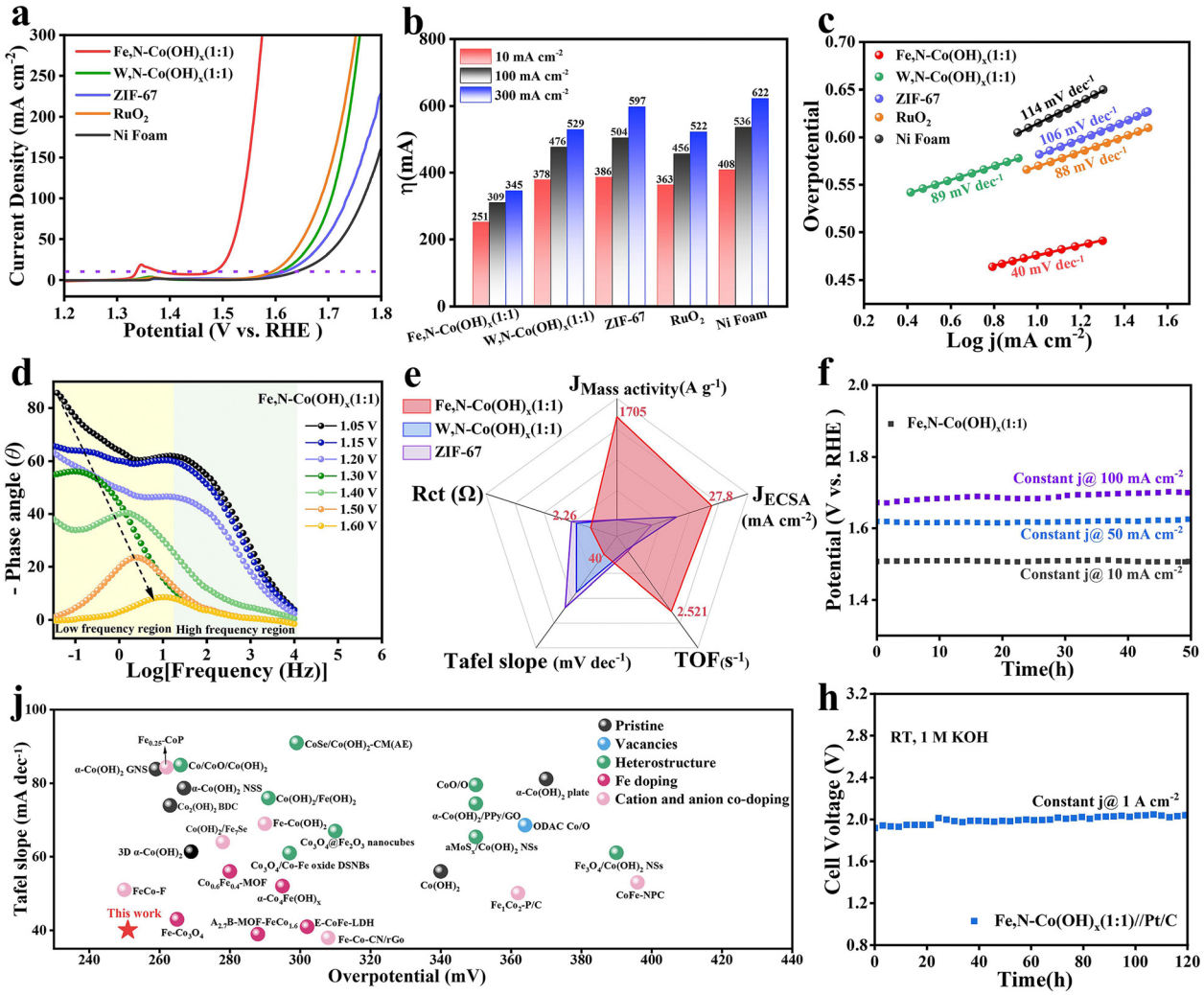

Fig. 3 Electrocatalytic OER activity evaluations. (a) LSV polarization curve in 1 M KOH solution at a scan rate of 5 mV s^{-1}. (b) Overpotential (η) at 10, 100, and 300 mA cm^{-2}. (c) Tafel slopes curve. (d) Bode plots for Fe,N–Co(OH)$_x$ (1 : 1) during the OER. (e) Comparison of OER activity between Fe,N–Co(OH)$_x$ (1 : 1) (red), W,N–Co(OH)$_x$ (1 : 1) (blue), and ZIF-67(orange-red). (f) Chronopotentiometric curve at 10, 50, and 100 mA cm^{-2}. (j) Comparison with recently reported catalysts. (h) The long-term durability of the prepared AEMWEs (Fe,N–Co(OH)$_x$ (1 : 1)//Pt/C) measured at 1 A cm^{-2} current density (operated at room temperature at a flow rate of 0.15 L min^{-1}).

performance of Fe,N–Co(OH)$_x$ (1 : 1) with previously reported catalysts, highlighting its superior performance.

2.3. Overall water splitting performance and post-characterization

Encouraged by the outstanding OER activity, an alkaline two-electrode electrolyzer was assembled using Fe,N–Co(OH)$_x$ (1 : 1) as the anode and 20 wt% commercial Pt/C as the cathode for overall water splitting (Fig. S28, ESI†). The Pt/C||Fe,N–Co(OH)$_x$ (1 : 1) system achieved a current density of 10 mA cm^{-2} at 1.58 V, which was lower than the industry-standard Pt/C||RuO_2 (1.76 V) (Fig. S28a, ESI†). Long-term stability tests over 50 h showed no significant voltage degradation (Fig. S28c, ESI†), thereby indicating good durability. The FE of Fe,N–Co(OH)$_x$ (1 : 1) was approximately 92.26% (Fig. S28b, ESI†). Benefitting from the well-behaved OER and overall water-splitting performance, the performance of anion-exchange membrane water electrolyzers (AEMWEs) has been further investigated. As shown in Fig. S29 (ESI†), the Fe,N–Co(OH)$_x$ (1 : 1)//Pt/C catalyzed electrolyzer requires only 1.98 V to achieve 1 A cm^{-2} current density, and outperforms RuO_2//Pt/C (2.42V). The stability of AEMWEs at room temperature (RT) was further tested (Fig. 3h). The results showed that Fe,N–Co(OH)$_x$ (1 : 1) was able to achieve an ultra-long stability of 120 h at a high current density of 1 A cm^{-2}. These suggested that Fe,N–Co(OH)$_x$ features excellent overall water-splitting performance, which will exhibit great potential in practical applications.

Post-characterization was performed following 50 h of OER using chronoamperometry. The XRD patterns before and after the stability test revealed no significant changes in the structure of the post-OER Fe,N–Co(OH)$_x$ (1 : 1) (Fig. S30, ESI†). ICP-MS measurements proved the Co and Fe contents in the post-OER Fe,N–Co(OH)$_x$ (1 : 1) were 40.1 wt% and 10.2 wt%, respectively (Table S2, ESI†). Furthermore, we tested the metal

content in the electrolyte after the OER. The concentrations of Fe and Co in the electrolyte after the OER were 0.00024 mg L^{-1} and 0.00137 mg L^{-1}, respectively, indicating that only $<0.03\%$ of the electrode metals were dissolved in the electrolyte. Thus, XRD and ICP analysis showed that Fe,N–Co(OH)$_x$ (1 : 1) maintained good structural stability and nearly no dissolution during the electrocatalytic tests. XPS analysis of post-OER Fe,N–Co(OH)$_x$ (1 : 1) is shown in Fig. S31 (ESI†). The Co 2p spectrum following the 50-hour durability test exhibited a negative shift of 0.4 eV, indicating an increased valence state (Fig. S31a, ESI†).[70] The Co 2p spectrum was deconvoluted into four prominent peaks corresponding to Co^{3+} (780.1 and 795.0 eV) and Co^{2+} (781.6 and 796.6 eV), along with four satellite peaks. The relative percentages of Fe^{2+} (60.8%) and Fe^{3+} (39.2%) in post-OER Fe,N–Co(OH)$_x$ (1 : 1) were almost unchanged compared to the original Fe,N–Co(OH)$_x$ (1 : 1) (Table S4, ESI†). Minimal change in the Fe 2p XPS spectra signified that Fe remained intact without dissolution following stability testing (Fig. S31b and Table S5, ESI†). The C 1s spectra showed peaks at 284.8, 288.5, 291.7, 292.8, and 295.4 eV, which were attributed to C═C, C═O, π═π, and C–F_x from Nafion,[71] respectively (Fig. S31e, ESI†). The proportion of the Co–N bond decreased from 20.78% to 11.65%, indicating a partial transformation from Co–N to Co–OH during surface reconstruction (Fig. S31c, d and Table S5, ESI†). Furthermore, the O 1s spectra revealed that the material retained a high proportion of O_v (27.4%) following 50 h of OER, indicating low O_v formation energy (Fig. S31d, ESI†). This indicated that lattice oxygen readily desorbed oxygen species to produce O_v and release O_2. Post-characterization confirmed that Fe,N co-doping effectively reduced O_v formation energy and synergistically activated the LOM pathway.

2.4. LOM mechanism

To demonstrate that the Fe,N–Co(OH)$_x$ (1 : 1) followed the LOM as the primary pathway, *in situ* ATR-FTIR measurements and *in situ* ^{18}O DEMS were conducted. A distinguishing feature of the LOM pathway was its involvement in the lattice oxygen desorption process (Step 5: OO* desorption, as shown in Fig. 5a) to form an O_v, commonly considered the rate-limiting step.[9,19,26] The *in situ* ATR-FTIR spectra for Fe,N–Co(OH)$_x$ (1 : 1) revealed a prominent absorption band at approximately 1100 cm^{-1}, corresponding to the O–O stretching mode of O_2^- on the catalyst surface (Fig. 4a).[72] This band reached its maximum intensity at 1.8 V. It disappeared when the voltage was lowered to 1.3 V, which indicated the dynamic adsorption and desorption of OO* species at the O_v site during the OER. In contrast, the vibrational band for O_2^- intermediates in W,N–Co(OH)$_x$ (1 : 1) appeared at 1.6 V, with weak peaks persisting between 1.6 and 1.8 V (Fig. 4b). This implied that W,N co-doping required higher voltages to drive OO* desorption, consistent with its poorer OER performance. Another absorption band for Fe,N–Co(OH)$_x$ (1 : 1) at 1250 cm^{-1} appeared between 1.3 and 1.8 V. This was attributed to the bending mode vibration of the absorbed OOH* intermediates.[72] At low potentials (1.1–1.7 V), the vibration of OOH* was relatively pronounced. Interestingly, as the potential increased to 1.8 V, the vibration of OOH* decreased while that of OO* increased. It suggests that the OOH* → OO* transition becomes more sufficient as the voltage increases, implying that the deprotonation of OOH* is rate-determining step (RDS). When the potential returned to 1.3 V, the conversion of OOH* to OO* was insufficient, so OOH* was reaccumulated. This finding indicates that introducing Fe lowered the reaction energy barrier and facilitated the deprotonation process of OOH* intermediates.[73]

The origin of the O–O bond configuration in the OO* intermediate for Fe,N–Co(OH)$_x$ (1 : 1) during the OER process was demonstrated through *in situ* ^{18}O isotope-labeled DEMS experiments, as shown in Fig. 4c. After Fe,N–Co(OH)$_x$ (1 : 1) was labeled with the isotope ^{18}O in 0.1 M $K^{18}OH$ (Step 2: lattice oxygen exchange, shown in Fig. 5a), three types of O_2 molecules were monitored by DEMS when tested in the 0.1 M $K^{16}OH$ electrolyte: $^{16}O^{16}O$, $^{16}O^{18}O$, and $^{18}O^{18}O$. The pronounced, high-intensity periodic signal of $^{16}O^{18}O$ (m/z = 34) provided strong evidence that the O–O bond configuration in Fe,N–Co(OH)$_x$ (1 : 1) originated from lattice oxygen during the OER process, thereby confirming that Fe,N–Co(OH)$_x$ (1 : 1) followed the LOM pathway.[74] Therefore, the *in situ* ATR-FTIR measurements and *in situ* ^{18}O isotope-labeled DEMS collectively provided compelling evidence that Fe,N co-doping activated lattice oxygen, with the LOM reaction mechanism being the primary pathway.

Subsequently, electrochemical *in situ* Raman spectroscopy was conducted to obtain deeper insight into the active structures of Fe,N–Co(OH)$_x$ (1 : 1) and W,N–Co(OH)$_x$ (1 : 1) during the OER (Fig. 4d and e). For Fe,N–Co(OH)$_x$ (1 : 1), two spectral features of $Co(OH)_2$ were observed at approximately 480 and 688 cm^{-1} at open circuit potential, corresponding to the E_g vibration modes of $Co(OH)_2$ (Fig. 4d).[75] As the voltage increased to 1.3 V, the A_{1g} vibration mode gradually disappeared, while new broadband emerged at 580 cm^{-1}, which was attributed to the E_g mode of the Co(III)–O band in CoOOH.[76] This peak narrowed and red-shifted to approximately 550 cm^{-1} as the voltage increased from 1.4 to 1.8 V, indicating a new phase associated with the A_{1g} vibration mode of the Co(IV)–O band in CoO_2.[18,77] This shift indicated that the strong PET from the N–Co–O–Fe moiety at the Fe,N–Co(OH)$_x$ (1 : 1) interface promoted the formation of high-valent Co(IV) species and involved active lattice oxygen in the OER. Moreover, no peaks related to Fe species were detected, indicating that Fe site was unlikely to be the active center in the Fe,N–Co(OH)$_x$ (1 : 1) catalyst. In contrast, W,N–Co(OH)$_x$ (1 : 1) exhibited CoOOH peaks at 580 cm^{-1} only when the applied potential ranged as 1.5–1.8 V (Fig. 4e). Notably, Fe,N–Co(OH)$_x$ (1 : 1) underwent a phase transition at a considerably lower potential (1.30 V), indicating that Fe,N co-doping accelerated the formation of CoOOH and CoO_2 species. Thus, *in situ* Raman revealed that the surface of the Fe,N–Co(OH)$_x$ (1 : 1) electrocatalyst reconstructed to CoOOH and CoO_2 with increasing voltage, with high-valent Co(IV) acting as the true active center.

2.5. Theoretical insights into the reaction mechanism

Based on *in situ* ATR-FTIR and ^{18}O isotope-labeled DEMS measurements, the LOM pathway was confirmed, and *in situ*

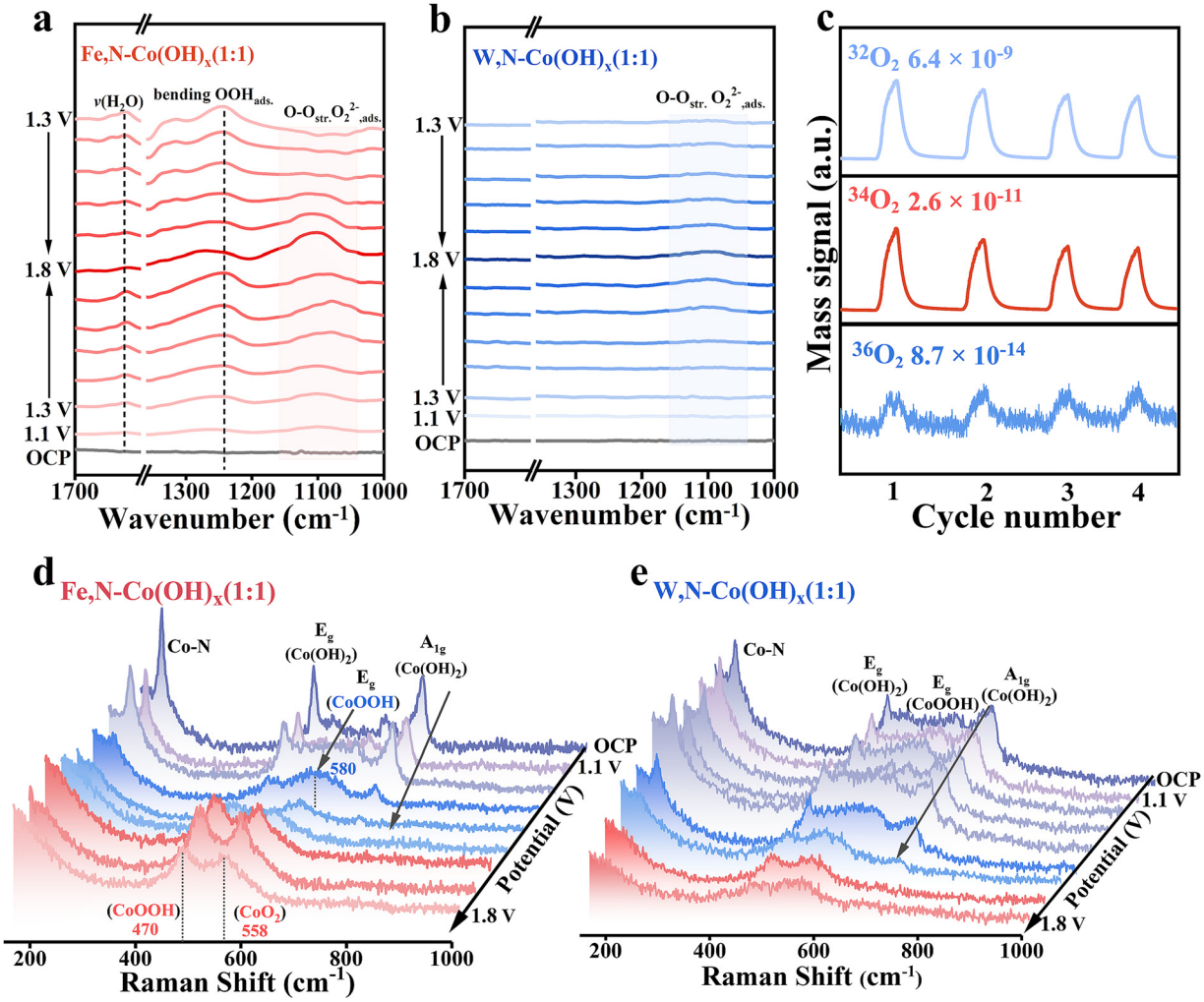

Fig. 4 Evidence for the LOM pathway. (a) and (b) *In situ* ATR-FTIR measurements in 1.0 M KOH across 1.1–1.8 V *vs.* RHE for (a) Fe,N–Co(OH)$_x$ (1 : 1) and (b) W,N–Co(OH)$_x$ (1 : 1). (c) ^{18}O isotope-labeled DEMS and the variations signals of $^{32}O_2$, $^{34}O_2$, and $^{36}O_2$ of Fe,N–Co(OH)$_x$ (1 : 1) in 0.1 M KOH. (d) and (e) *In situ* Raman in 1.0 M KOH across 1.1–1.8 V *vs.* RHE for (d) Fe,N–Co(OH)$_x$ (1 : 1) and (e) W,N–Co(OH)$_x$ (1 : 1).

Raman spectroscopy identified the true active site. Co(OH)$_2$ based materials contained trimetal-surrounded lattice oxygen acting as the site for the LOM, as shown in Fig. 5a. Three slab models were analyzed: Co, CoN, and FeCoN sites (Fig. 5b), representing undoped, N-doped, and Fe,N co-doped conditions, respectively. The electron flow within the N–Co–O–Fe structure is further illustrated by the charge difference map (Fig. 5b). The introduction of N at the CoN site really weakens the electron cloud density at the adjacent Co atoms compared to the Co site (Fig. 4b, purple circles). However, as shown at the FeCoN site, Fe,N co-doping facilitated electron transfer from Co to Fe atoms. Consequently, the electrons of the OO* species could be preferentially transferred to Fe, which is more favorable for OO* desorption and enhanced O_v formation. The Gibbs free energy diagrams of Fe,N–Co(OH)$_x$ (1 : 1) with an exposed (100) plane were calculated and are presented in Fig. 5c and d, with an applied potential of 1.23 V. The diagrams included the O_v as the initial site and OH*, O*, OOH*, and OO* intermediates. As shown in Fig. 5d, the Co site exhibited a high OO* desorption energy (3.47 eV) at Step 5 of lattice O_v formation, thereby indicating a limited LOM pathway. The OO* desorption step was the rate-limiting step, consistent with reported calculations for unmodified LDH materials.[19] With N-doping, the OO* desorption energy at the CoN site decreased to 2.48 eV but remained a rate-limiting step. Following Fe,N co-doping, the rate-limiting step at the FeCoN site shifted from OO* desorption (reduced sharply to 0.43 eV) to H desorption of OOH* (overpotential η = 0.81 eV). This was consistent with the *in situ* ATR-FTIR findings, which indicated that the OOH* intermediate species were a part of the rate-limiting step. For OH* adsorption, an increase in the proportion of Fe^{3+} would theoretically favor OH* adsorption.[67] However, overly strong adsorption of oxygen intermediates is unfavorable to subsequent OO* desorption. The introduction of N could well modulate OH* adsorption. The adsorption energy of OH* for the FeCoN site (−1.53 eV) and the CoN site (−1.74 eV) was lower than Co site (−2.74 eV) (Fig. 5d). The OH* adsorption step is a spontaneous and non-rate-limiting step, a properly weakened

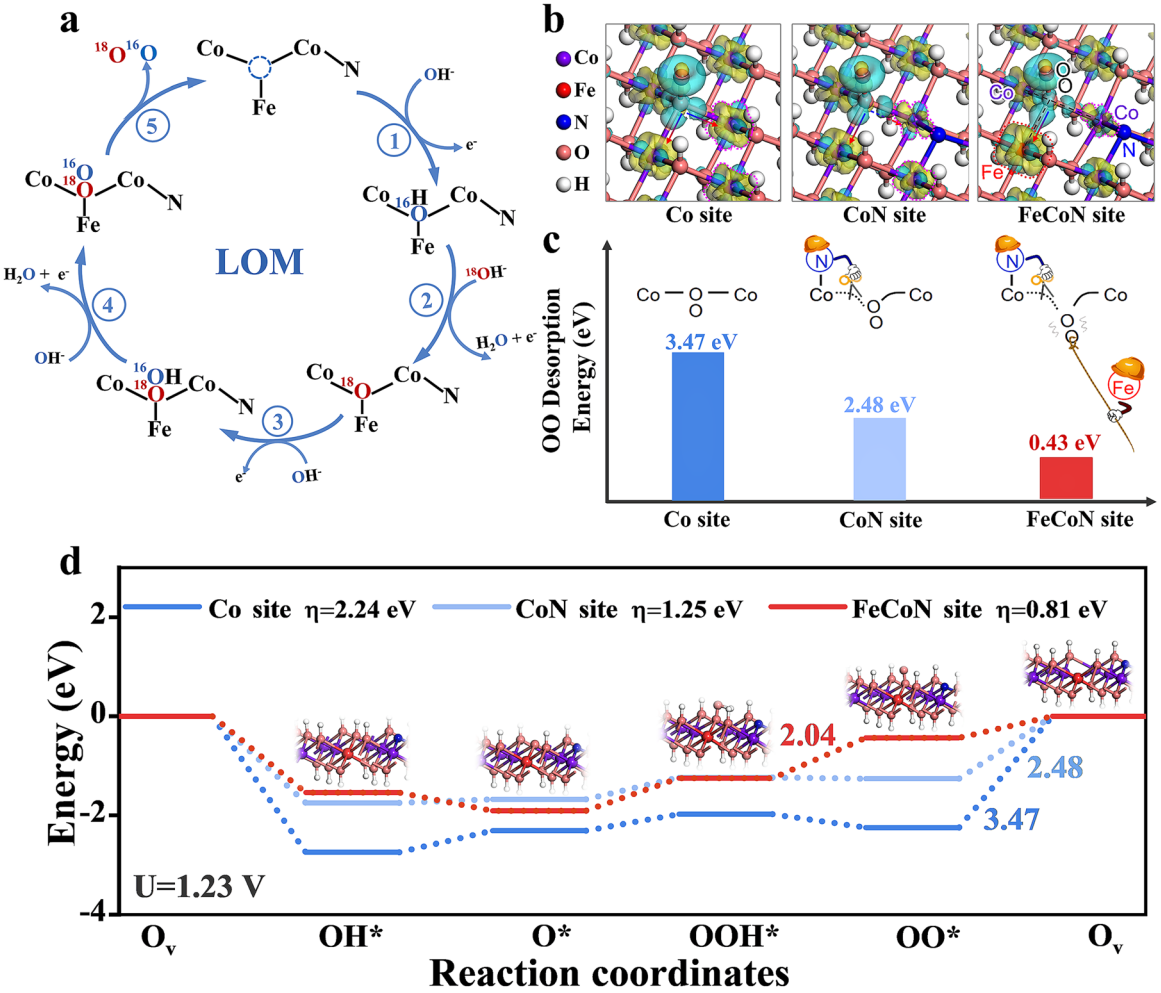

Fig. 5 Mechanism of LOM path activation by Fe,N co-doping. (a) Schematic of LOM mechanism. (b) Structural diagrams and charge density difference analysis for Co, CoN, and FeCoN sites, where the yellow and blue regions indicate electronic accumulation and depletion, respectively. (c) Schematic of Fe,N co-doping reducing the OO* desorption energy. (d) Gibbs free energy diagrams of the LOM pathway on a lattice oxygen site. Including all oxygen intermediates OH*, O*, OOH*, OO* and O_v at the FeCoN site.

adsorption is more conducive to balancing the energy barrier potential of the overall reaction. Therefore, Fe,N co-doping could optimize *OH adsorption and reduce the OO* desorption energy (Fig. 5c), consequently activating the LOM pathway.

To rationally design Fe and N co-doped defects, we analyzed the impact of Fe and N locations on OER activity. Three Fe locations (Fig. S32, ESI†) were examined. The Fe_1 site corresponded to the previously discussed FeCoN sites, which exhibited an overpotential of 0.81 eV. The rate-determining steps for Fe_2 site and Fe_3 site were not shifted from OO* desorption to other reaction steps, with η values of 2.15 and 2.53 eV, respectively (Fig. S33, ESI†). The OO* desorption energies for the Fe_1 site (0.43 eV) and the Fe_2 site (0.92 eV) were substantially lower than that for the Fe_3 site (1.30 eV). The key distinction of the Fe_3 site was that N was bonded to Fe rather than Co. Therefore, for optimal activity with Fe and N co-doping, N must form as many Co–N bonds as possible. In our synthesis strategy, Fe was incorporated through Fe electrode sputtering, whereas N was pre-coordinated with Co in the solution. This approach minimized the formation of Fe–N bonds, thereby ensuring that Co–N bonds were the dominant metal–N coordination. The impact of N locations on the OER pathway was also analyzed (Fig. S34–S37, ESI†). The CoN_2 configuration exhibited a higher OO* desorption energy (1.63 eV) compared to the CoN_1 site (1.25 eV) and the FeCoN site (0.43 eV). This analysis confirmed that Fe and N synergistically reduced OO* desorption energy, promoted O_v formation and activated the LOM pathway. For designing multi-structures, the prioritization of Co–N coordination while minimizing Fe–N coordination is essential to construct lattice oxygen-participating in the N–Co–O–Fe active site.

3. Conclusions

This study synthesized metallic Fe and nonmetallic N co-doped $Co(OH)_2$ (*i.e.*, Fe,N–$Co(OH)_x$) as an OER catalyst using plasma discharge in water. This facilitated the simultaneous generation of multiple O vacancies, thereby significantly enhancing

the intrinsic activity of $Co(OH)_2$. Fe,N–$Co(OH)_x$ demonstrated high mass activity (1705 A g_{metal}^{-1}) and high TOF(2.521 s^{-1}), which were 80.4 and 57 times higher than those of W,N–$Co(OH)_x$ (21.2 A g_{metal}^{-1} and 0.044 s^{-1}), respectively. *In situ* and *ex situ* EIS and *in situ* Raman revealed that Fe-doping improves the electrical conductivity, facilitates the electron transfer ability, and accelerates surface remodeling. DFT calculations revealed that N doping can modulate OH* adsorption and reduce OO* desorption energy. The co-doping with metallic Fe and nonmetallic N facilitated the formation of N–Co–O–Fe moiety molecules at the Fe,N–$Co(OH)_x$ interface. XPS, XAS, PDOS, and *in situ* Raman analyses indicated that the N–Co–O–Fe moiety at the Fe,N–$Co(OH)_x$ interface facilitated electron transfer from Co to Fe and promoted the formation of active high-valent Co(IV) species. This increased the metal–O covalency and optimized the adsorption and desorption of oxygen intermediates. The OO* intermediate was observed *via in situ* ATR-FTIR and *in situ* DEMS, which confirmed the activation of lattice oxygen in Fe,N–$Co(OH)_x$ (1 : 1), thereby supporting the LOM mechanism on active oxygen vacancy sites. Detailed investigations and DFT calculations demonstrated that Fe,N co-doping effectively tuned the d-band center of the active site. Furthermore, the LOM mechanism on lattice oxygen sites reduced the adsorption-free energy of O_2 desorption in the rate-limiting steps of the OER process, thereby highlighting the substantial contribution of multiple defects to the improved OER performance.

Author contributions

Q. Yang, Z. Y. Wang, F. Yu designed the catalyst synthesis and performed electrochemical experiments, characterized the catalyst and analyzed the data, as well as wrote the article. Q. Yang, Y. A. Li, Y. X. Wu designed and performed DFT calculations., and designed the flowchart. Q. Yang, Y. X. Li, Y. X. Wu, together performed the *in situ* ATR-FTIR and further characterization studies. C. X. Yang, L. L. Ban, Y. X. Zhao assisted experiments and experimental analyses. H. Pang, Y. X. Wu, B. Dai, G. Wang, Y. S. Li, J. L. Zhang performed experimental conceptualization and assisted in data analysis. F. Yu, Z. Y. Wang conceived and designed the experiments, supervised the execution of the overall project, provided laboratory space and instrumentation, and financed the experiments. All the authors discussed the results and reviewed the manuscript.

Data availability

The data supporting this article have been included as part of the ESI.†

Conflicts of interest

The authors declare that they have no known competing financial interests or personal relationships that could have appeared to influence the work reported in this paper.

Acknowledgements

This work was financially supported by the National Natural Science Foundation of China (No. 12205207), the Xinjiang Science and Technology Program (No. 2023TSYCCX0118), and the Bingtuan Science and Technology Program (No. 2023AB033 and 2024DA038).

Notes and references

1 M. Chatenet, B. G. Pollet, D. R. Dekel, F. Dionigi, J. Deseure, P. Millet, R. D. Braatz, M. Z. Bazant, M. Eikerling, I. Staffell, P. Balcombe, Y. Shao-Horn and H. Schäfer, *Chem. Soc. Rev.*, 2022, **51**, 4583–4762.
2 N. Han, W. Zhang, W. Guo, H. Pan, B. Jiang, L. Xing, H. Tian, G. Wang, X. Zhang and J. Fransaer, *Nano-Micro Lett.*, 2023, **15**, 185.
3 P. Roy Chowdhury, H. Medhi, K. G. Bhattacharyya and C. Mustansar Hussain, *Coord. Chem. Rev.*, 2023, **483**, 215083.
4 A. Grimaud, A. Demortière, M. Saubanère, W. Dachraoui, M. Duchamp, M.-L. Doublet and J.-M. Tarascon, *Nat. Energy*, 2016, **2**, 16189.
5 Z. W. Seh, J. Kibsgaard, C. F. Dickens, I. Chorkendorff, J. K. Nørskov and T. F. Jaramillo, *Science*, 2017, **355**, eaad4998.
6 J. H. Montoya, L. C. Seitz, P. Chakthranont, A. Vojvodic, T. F. Jaramillo and J. K. Nørskov, *Nat. Mater.*, 2017, **16**, 70–81.
7 M. J. Craig, G. Coulter, E. Dolan, J. Soriano-López, E. Mates-Torres, W. Schmitt and M. García-Melchor, *Nat. Commun.*, 2019, **10**, 4993.
8 A. Grimaud, O. Diaz-Morales, B. Han, W. T. Hong, Y.-L. Lee, L. Giordano, K. A. Stoerzinger, M. T. M. Koper and Y. Shao-Horn, *Nat. Chem.*, 2017, **9**, 457–465.
9 X. Chen, Q. Wang, Y. Cheng, H. Xing, J. Li, X. Zhu, L. Ma, Y. Li and D. Liu, *Adv. Funct. Mater.*, 2022, **32**, 2112674.
10 P. Ye, K. Fang, H. Wang, Y. Wang, H. Huang, C. Mo, J. Ning and Y. Hu, *Nat. Commun.*, 2024, **15**, 1012.
11 P. Wang, Q. Cheng, C. Mao, W. Su, L. Yang, G. Wang, L. Zou, Y. Shi, C. Yan, Z. Zou and H. Yang, *J. Power Sources*, 2021, **502**, 229903.
12 Z.-F. Huang, J. Song, Y. Du, S. Xi, S. Dou, J. M. V. Nsanzimana, C. Wang, Z. J. Xu and X. Wang, *Nat. Energy*, 2019, **4**, 329–338.
13 C. Wang, P. Zhai, M. Xia, W. Liu, J. Gao, L. Sun and J. Hou, *Adv. Mater.*, 2023, **35**, 2209307.
14 H. G. Xu, C. Zhu, H. Y. Lin, J. K. Liu, Y. X. Wu, H. Q. Fu, X. Y. Zhang, F. Mao, H. Y. Yuan, C. Sun, P. F. Liu and H. Yang, *Angew. Chem., Int. Ed.*, 2024, e202415423.
15 A. Pei, P. Wang, S. Zhang, Q. Zhang, X. Jiang, Z. Chen, W. Zhou, Q. Qin, R. Liu, R. Du, Z. Li, Y. Qiu, K. Yan, L. Gu, J. Ye, G. I. N. Waterhouse, W.-H. Huang, C.-L. Chen, Y. Zhao and G. Chen, *Nat. Commun.*, 2024, **15**, 5899.
16 G. Chen, C. Xu, X. Huang, J. Ye, L. Gu, G. Li, Z. Tang, B. Wu, H. Yang, Z. Zhao, Z. Zhou, G. Fu and N. Zheng, *Nat. Mater.*, 2016, **15**, 564–569.

17 D. Zhou, J. Yu, J. Tang, X.-Y. Li and P. Ou, *Adv. Energy Mater.*, 2024, 2404007.
18 Y. Zhang, W. Zhang, X. Zhang, Y. Gao, Q. Zhao, J. Li and G. Liu, *Small*, 2024, 2405080.
19 Z. He, J. Zhang, Z. Gong, H. Lei, D. Zhou, N. Zhang, W. Mai, S. Zhao and Y. Chen, *Nat. Commun.*, 2022, **13**, 2191.
20 A. Grimaud, W. T. Hong, Y. Shao-Horn and J. M. Tarascon, *Nat. Mater.*, 2016, **15**, 121–126.
21 F. Sun, L. Li, G. Wang and Y. Lin, *J. Mater. Chem. A*, 2017, **5**, 6849–6859.
22 F. Dionigi, J. Zhu, Z. Zeng, T. Merzdorf, H. Sarodnik, M. Gliech, L. Pan, W.-X. Li, J. Greeley and P. Strasser, *Angew. Chem., Int. Ed.*, 2021, **60**, 14446–14457.
23 J.-Y. Zhang, Y. Yan, B. Mei, R. Qi, T. He, Z. Wang, W. Fang, S. Zaman, Y. Su, S. Ding and B. Y. Xia, *Energy Environ. Sci.*, 2021, **14**, 365–373.
24 S.-H. Ye, Z.-X. Shi, J.-X. Feng, Y.-X. Tong and G.-R. Li, *Angew. Chem., Int. Ed.*, 2018, **57**, 2672–2676.
25 C. Gong, L. Zhao, D. Li, X. He, H. Chen, X. Du, D. Wang, W. Fang, X. Zeng and W. Li, *Chem. Eng. J.*, 2023, **466**, 143124.
26 Y. Zhang, J. Kang, H. Xie, H. Yin, Z. Zhang, E. Liu, L. Ma, B. Chen, J. Sha, L. Qian, W. Hu, C. He and N. Zhao, *Appl. Catal., B*, 2024, **341**, 123331.
27 W. Huang, J. Li, X. Liao, R. Lu, C. Ling, X. Liu, J. Meng, L. Qu, M. Lin, X. Hong, X. Zhou, S. Liu, Y. Zhao, L. Zhou and L. Mai, *Adv. Mater.*, 2022, **34**, 2200270.
28 Y. Wang, C. Xie, Z. Zhang, D. Liu, R. Chen and S. Wang, *Adv. Funct. Mater.*, 2018, **28**, 1703363.
29 C. Lyu, Y. Li, J. Cheng, Y. Yang, K. Wu, J. Wu, H. Wang, W.-M. Lau, Z. Tian, N. Wang and J. Zheng, *Small*, 2023, **19**, 2302055.
30 H.-J. Qiu, P. Du, K. Hu, J. Gao, H. Li, P. Liu, T. Ina, K. Ohara, Y. Ito and M. Chen, *Adv. Mater.*, 2019, **31**, 1900843.
31 G. Panomsuwan, N. Saito and T. Ishizaki, *ACS Appl. Mater. Interfaces*, 2016, **8**, 6962–6971.
32 Y. Xing, C. Wang, D. Li, R. Wang, S. Liang, Y. Li, Y. Liu and X. Zhang, *Adv. Funct. Mater.*, 2022, **32**, 2207694.
33 K. Lu, Z. Wang, Y. Wu, X. Zhai, C. Wang, J. Li, Z. Wang, X. Li, Y. He, T. An, K. Yang, D. Yang, F. Yu and B. Dai, *Chem. Eng. J.*, 2023, **451**, 138590.
34 K. Lu, Z. Wang, B. Dai, Y. Han, X. Chen, J. Yu, K. Yang, D. Yang, C. Ma and F. Yu, *Chem. Eng. J.*, 2022, **431**, 133246.
35 D. Zha, R. Wang, S. Tian, Z.-J. Jiang, Z. Xu, C. Qin, X. Tian and Z. Jiang, *Nano-Micro Lett.*, 2024, **16**, 250.
36 S. Sanati, A. Morsali and H. García, *Energy Environ. Sci.*, 2022, **15**, 3119–3151.
37 A. Hameed, M. Batool, Z. Liu, M. A. Nadeem and R. Jin, *ACS Energy Lett.*, 2022, **7**, 3311–3328.
38 D. Li, Y. Xing, R. Yang, T. Wen, D. Jiang, W. Shi and S. Yuan, *ACS Appl. Mater. Interfaces*, 2020, **12**, 29253–29263.
39 X. Jia, Y. Zhao, G. Chen, L. Shang, R. Shi, X. Kang, G. I. N. Waterhouse, L.-Z. Wu, C.-H. Tung and T. Zhang, *Adv. Energy Mater.*, 2016, **6**, 1502585.
40 J. Qian, F. Sun and L. Qin, *Mater. Lett.*, 2012, **82**, 220–223.
41 F. Liu and Z. Fan, *Chem. Soc. Rev.*, 2023, **52**, 1723–1772.
42 X. Zhang, Z. Chen, M. Jiao, X. Ma, K. Mou, F. Cheng, Z. Wang, X. Zhang and L. Liu, *Appl. Catal., B*, 2020, **279**, 119383.
43 L. Dubau, J. Nelayah, S. Moldovan, O. Ersen, P. Bordet, J. Drnec, T. Asset, R. Chattot and F. Maillard, *ACS Catal.*, 2016, **6**, 4673–4684.
44 J. Fu, F. M. Hassan, C. Zhong, J. Lu, H. Liu, A. Yu and Z. Chen, *Adv. Mater.*, 2017, **29**, 1702526.
45 Z. Liu, R. Ma, M. Osada, K. Takada and T. Sasaki, *J. Am. Chem. Soc.*, 2005, **127**, 13869–13874.
46 Q. Wang, S. Tang, Z. Wang, J. Wu, Y. Bai, Y. Xiong, P. Yang, Y. Wang, Y. Tan, W. Liu, X. Xiong and Y. Lei, *Adv. Funct. Mater.*, 2023, **33**, 2307390.
47 P. Gao, Y. Zeng, P. Tang, Z. Wang, J. Yang, A. Hu and J. Liu, *Adv. Funct. Mater.*, 2022, **32**, 2108644.
48 J. Qin, S. Wang and X. Wang, *Appl. Catal., B*, 2017, **209**, 476–482.
49 J. Bao, X. Zhang, B. Fan, J. Zhang, M. Zhou, W. Yang, X. Hu, H. Wang, B. Pan and Y. Xie, *Angew. Chem., Int. Ed.*, 2015, **54**, 7399–7404.
50 D. Zhou, F. Li, Y. Zhao, L. Wang, H. Zou, Y. Shan, J. Fu, Y. Ding, L. Duan, M. Liu, L. Sun and K. Fan, *ACS Catal.*, 2023, **13**, 4398–4408.
51 Z. Öztürk, M. Filez and B. M. Weckhuysen, *Chem. – Eur. J.*, 2017, **23**, 10915–10924.
52 H. Zhang, Q. Jiang, J. H. L. Hadden, F. Xie and D. J. Riley, *Adv. Funct. Mater.*, 2021, **31**, 2008989.
53 Y. Tian, M. Li, Z. Wu, Q. Sun, D. Yuan, B. Johannessen, L. Xu, Y. Wang, Y. Dou, H. Zhao and S. Zhang, *Angew. Chem., Int. Ed.*, 2022, **61**, e202213296.
54 X. Zhang, H. Zhong, Q. Zhang, Q. Zhang, C. Wu, J. Yu, Y. Ma, H. An, H. Wang, Y. Zou, C. Diao, J. Chen, Z. G. Yu, S. Xi, X. Wang and J. Xue, *Nat. Commun.*, 2024, **15**, 1383.
55 Y. Chen, X.-Y. Li, Z. Chen, A. Ozden, J. E. Huang, P. Ou, J. Dong, J. Zhang, C. Tian, B.-H. Lee, X. Wang, S. Liu, Q. Qu, S. Wang, Y. Xu, R. K. Miao, Y. Zhao, Y. Liu, C. Qiu, J. Abed, H. Liu, H. Shin, D. Wang, Y. Li, D. Sinton and E. H. Sargent, *Nat. Nanotechnol.*, 2024, **19**, 311–318.
56 L. Zhuang, L. Ge, H. Liu, Z. Jiang, Y. Jia, Z. Li, D. Yang, R. K. Hocking, M. Li, L. Zhang, X. Wang, X. Yao and Z. Zhu, *Angew. Chem., Int. Ed.*, 2019, **58**, 13565–13572.
57 Y. Zhai, X. Ren, Y. Sun, D. Li, B. Wang and S. Liu, *Appl. Catal., B*, 2023, **323**, 122091.
58 J. Y. C. Chen, L. Dang, H. Liang, W. Bi, J. B. Gerken, S. Jin, E. E. Alp and S. S. Stahl, *J. Am. Chem. Soc.*, 2015, **137**, 15090–15093.
59 N. Zhang, X. Feng, D. Rao, X. Deng, L. Cai, B. Qiu, R. Long, Y. Xiong, Y. Lu and Y. Chai, *Nat. Commun.*, 2020, **11**, 4066.
60 Y.-N. Zhou, F.-T. Li, B. Dong and Y.-M. Chai, *Energy Environ. Sci.*, 2024, **17**, 1468–1481.
61 C. Y. Huang, H. M. Lin, C. H. Chiang, H. A. Chen, T. R. Liu, S. K. D. Vishnu, J. W. Chiou, R. Sankar, H. M. Tsai, W. F. Pong and C. W. Chen, *Adv. Funct. Mater.*, 2023, **33**, 2305792.
62 J. Li, D. Chu, H. Dong, D. R. Baker and R. Jiang, *J. Am. Chem. Soc.*, 2020, **142**, 50–54.
63 J. Hao, W. Yang, Z. Peng, C. Zhang, Z. Huang and W. Shi, *ACS Catal.*, 2017, **7**, 4214–4220.

64 W. T. Hong, K. A. Stoerzinger, Y.-L. Lee, L. Giordano, A. Grimaud, A. M. Johnson, J. Hwang, E. J. Crumlin, W. Yang and Y. Shao-Horn, *Energy Environ. Sci.*, 2017, **10**, 2190–2200.
65 M. Saubanère, E. McCalla, J. M. Tarascon and M. L. Doublet, *Energy Environ. Sci.*, 2016, **9**, 984–991.
66 X. Cheng, E. Fabbri, M. Nachtegaal, I. E. Castelli, M. El Kazzi, R. Haumont, N. Marzari and T. J. Schmidt, *Chem. Mater.*, 2015, **27**, 7662–7672.
67 Z. Du, Z. Meng, X. Gong, Z. Hao, X. Li, H. Sun, X. Hu, S. Yu and H. Tian, *Angew. Chem., Int. Ed.*, 2024, **63**, e202317022.
68 J. Hwang, R. R. Rao, L. Giordano, Y. Katayama, Y. Yu and Y. Shao-Horn, *Science*, 2017, **358**, 751–756.
69 W. Chen, B. Wu, Y. Wang, W. Zhou, Y. Li, T. Liu, C. Xie, L. Xu, S. Du, M. Song, D. Wang, Y. liu, Y. Li, J. Liu, Y. Zou, R. Chen, C. Chen, J. Zheng, Y. Li, J. Chen and S. Wang, *Energy Environ. Sci.*, 2021, **14**, 6428–6440.
70 J. Yang, H. Liu, W. N. Martens and R. L. Frost, *J. Phys. Chem. C*, 2010, **114**, 111–119.
71 M. C. Militello and S. W. Gaarenstroom, *Surf. Sci. Spectra*, 2005, **10**, 117–126.
72 S. Mondal, D. Bagchi, M. Riyaz, S. Sarkar, A. K. Singh, C. P. Vinod and S. C. Peter, *J. Am. Chem. Soc.*, 2022, **144**, 11859–11869.
73 Y. Hao, S.-F. Hung, C. Tian, L. Wang, Y.-Y. Chen, S. Zhao, K.-S. Peng, C. Zhang, Y. Zhang, C.-H. Kuo, H.-Y. Chen and S. Peng, *Angew. Chem., Int. Ed.*, 2024, **63**, e202402018.
74 X. Ren, Y. Zhai, N. Yang, B. Wang and S. Liu, *Adv. Funct. Mater.*, 2024, **34**, 2401610.
75 B. Sun, S. Zhang, H. Yang, T. Zhang, Q. Dong, W. Zhang, J. Ding, X. Liu, L. Wang, X. Han and W. Hu, *Adv. Funct. Mater.*, 2024, **34**, 2315862.
76 Z. Kou, Y. Yu, X. Liu, X. Gao, L. Zheng, H. Zou, Y. Pang, Z. Wang, Z. Pan, J. He, S. J. Pennycook and J. Wang, *ACS Catal.*, 2020, **10**, 4411–4419.
77 C. Jing, T. Yuan, L. Li, J. Li, Z. Qian, J. Zhou, Y. Wang, S. Xi, N. Zhang, H.-J. Lin, C.-T. Chen, Z. Hu, D.-W. Li, L. Zhang and J.-Q. Wang, *ACS Catal.*, 2022, **12**, 10276–10284.